



Degradation of Reactive Orange 16 Dye With Heterogeneous Fenton Process Using Magnetic Nano-Sized Clay as Catalyst: A Central Composite Optimization Study

Reaktif Turuncu 16 Boyasınının, Katalizör Olarak Manyetik Nano Boyutlu Kil Kullanılarak Heterojen Fenton Prosesi ile Parçalanması: Bir Merkezi Kompozit Optimizasyon Çalışması

Dilara Öztürk[✉]

Department of Environmental Engineering, Faculty of Engineering, Van Yuzuncu Yil University, Van, Turkey.

ABSTRACT

In this study, Fe_3O_4 /montmorillonite was synthesized as a heterogeneous Fenton catalyst to remove Reactive Orange 16 from aqueous solutions based on chemical oxygen demand. System parameters such as H_2O_2 concentration, catalyst dose, pH, and reaction time were numerically optimized based on Central Composite Design. The catalyst was characterized with X-ray diffraction, Fourier transform infrared spectroscopy, scanning electron microscopy, energy-dispersive X-ray spectroscopy, transmission electron microscopy, dynamic light scattering, ζ potential, and Brunauer-Emmett-Teller. The adsorption process contributed to the removal of Reactive Orange 16, but the heterogeneous Fenton process had a higher share and occurred faster than the adsorption process. Optimum conditions were determined as catalyst dosage: 1.83 (g/L), H_2O_2 concentration: 77.98 (mM), pH: 3, and reaction time: 60 min. Under these conditions, chemical oxygen demand removal efficiency estimated from the model was 84.82% and found experimentally was 85.90%. Successful removal of Reactive Orange 16 from aqueous environments is possible with a heterogeneous Fenton process using Fe_3O_4 /montmorillonite.

Key Words

Fe_3O_4 /montmorillonite, anionic dye, heterogeneous Fenton, optimization.

ÖZ

Bu çalışmada Fe_3O_4 /montmorillonit, sulu çözeltilerden Reaktif Turuncu 16'nın kimyasal oksijen ihtiyacı'na dayalı uzaklaştırılması için heterojen bir fenton katalizörü olarak sentezlenmiştir. H_2O_2 konsantrasyonu, katalizör dozu, pH ve reaksiyon süresi gibi sistem parametreleri, Merkezi kompozit tasarım temelinde sayısal olarak optimize edildi. Katalizör, X-ışını kırınımı, Fourier dönüşümlü kızılötesi spektroskopisi, Taramalı elektron mikroskopu, Enerji dağılımlı X-ışını spektroskopisi, Transmisyon elektron mikroskopu, Dinamik ışık saçılımı, ζ potansiyeli ve Brunauer-Emmett-Teller ile karakterize edildi. Adsorpsiyon prosesi, Reaktif Turuncu 16'nın uzaklaştırılmasında katkıda bulundu, ancak heterojen Fenton prosesi büyük bir paya sahipti ve adsorpsiyon prosesinden daha hızlı gerçekleşti. Optimum koşullar katalizör dozajı: 1.83 (g/L), H_2O_2 konsantrasyonu: 77.98 (mM), pH: 3 ve reaksiyon süresi: 60 dakika olarak belirlendi. Bu koşullar altında kimyasal oksijen ihtiyacı giderim verimi modelden % 84.82 olarak tahmin edildi ve deneysel olarak % 85.90 bulundu. Reaktif Turuncu 16'nın sulu ortamlardan başarılı bir şekilde uzaklaştırılması Fe_3O_4 /montmorillonit kullanılarak heterojen Fenton prosesi ile mümkündür.

Anahtar Kelimeler

Fe_3O_4 /montmorillonit, anyonik boya, heterojen Fenton, optimizasyon

Article History: Received: May 17, 2021; Revised: Aug 2, 2021; Accepted: Dec 15, 2021; Available Online: Feb 28, 2021.

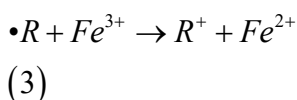
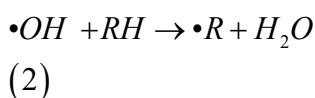
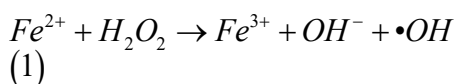
DOI: <https://doi.org/10.15671/hjbc.937728>

Correspondence to: D. Ozturk, Department of Environmental Engineering, Faculty of Engineering, Van Yuzuncu Yil University, Van, Turkey.

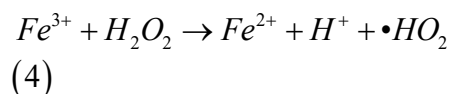
E-Mail: dozturk@yyu.edu.tr

INTRODUCTION

Recently, the increase in the use of dyestuffs in areas from the food industry to the textile, pharmaceutical industry, and furniture industry is not only a visible pollution factor in wastewater, but removal has also become a current problem. Dyestuffs affect photosynthetic life indirectly by reducing light transmission in recipient environments [1]. Moreover, these wastewaters containing toxic chemicals for living life threaten organisms in the receiving environment and accumulate in plants due to soil pollution and therefore pose an eco-toxicological risk by being included in animal and human nutrition. By penetrating from the soil surface, they mix with groundwater. According to their chemical structure, dyes are categorized as azo, diazo, basic, acidic, etc. Reactive Orange 16 (RO16) is an anionic azo dye [2]. Azo dyes are known for their high solubility in water and difficult biodegradability. This situation emphasizes the importance of effective removal methods for azo dyes. Effective processes such as adsorption [3], electrochemical oxidation [4], electrocoagulation [5], membrane applications [6], and Fenton oxidation [7,8] are used for the removal of dyes. However, each process has handicaps such as energy consumption, secondary waste generation, chemical consumption problems for electrochemical processes, coagulation techniques, and chemical processes, respectively [9]. Oxidation processes stand out in terms of generally not creating toxic by-products. Some studies found very effective results for organic pollutants, especially dye wastewaters, using Fenton processes [10–12]. Fenton processes are mainly based on the degradation of pollutants by oxidants formed as a result of the reaction of Fe^{2+} salts and H_2O_2 (Eqs. (1-3) [13,14]). Here Fe^{2+} acts as the initiator of the reaction, catalyzing the conversion of H_2O_2 to hydroxyl radicals ($\bullet OH$). Hydroxyl radicals ($\bullet OH$) convert organic pollutants (RH) into organic radicals ($\bullet R$) and oxidation by-products. Organic radicals ($\bullet R$) react with Fe^{3+} to form Fe^{2+} again.



The waste sludge that occurs due to Fe^{2+} in Fenton processes is one of the disadvantages of the homogeneous Fenton process. One of the factors limiting the applicability of Fenton processes on an industrial scale is costly Fe^{2+} and H_2O_2 consumption. The high amount of chemical consumption during the reduction of Fe^{3+} to Fe^{2+} with H_2O (Eq.4) [15] is known as the major disadvantage of homogeneous Fenton systems. On the other hand, homogeneous Fenton processes produce large amounts of iron sludge in highly acidic conditions, which can be considered among other disadvantages.



Hence, the need to use a cost-effective catalyst has emerged. Heterogeneous Fenton and heterogeneous Fenton-like processes have attracted attention, as Fe^{3+} salts have lower costs than Fe^{2+} salts, and other metal-based catalysts were investigated. Synthesized catalysts such as carbon nanotube-based ferrihydrite [16], clay supported Fe_3O_4 [17], and biochar modified $CuFeO_2$ [18] were used for these processes.

Montmorillonite (MMT) is mostly a clay group with a smectite structure. Smectite structures have two inward silica layers [19,20] and a gibbsite layer compressed into these layers [21], and an Al octahedral layer is present in the centre of this layer. MMTs, which can be found in many parts of the world, are found quite widely in Turkey.

In this study, montmorillonite (MMT) obtained from the Erzurum/Horasan region in Turkey was used for the synthesis of nano-sized Fe_3O_4 . The produced magnetic clay was characterized and investigated as a heterogeneous Fenton catalyst for the removal of RO16 from aqueous solutions based on chemical oxygen demand (COD) removal. Optimization of system inputs such as catalyst dosage, H_2O_2 concentration, reaction time, and solution pH was performed numerically based on Central Composite modelling.

Although clay-based Fe_3O_4 catalysts have been used for dye removal, as far as the author is aware, there is no heterogeneous Fenton study that handled RO16 degradation with an MMT-based nano Fe_3O_4 catalyst and optimized multi-system parameters numerically.



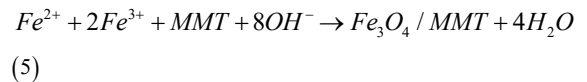
Figure 1. (a) Pretreated MMT samples and (b) produced magnetic Fe_3O_4/MMT .

MATERIALS and METHODS

Preparation of catalyst and dye properties

MMT samples obtained from Erzurum/Horasan region were washed several times with ultrapure water to remove impurities and dried in the oven at 50 °C for 24 h. The dried samples were prepared for the next stage by sieving them through 250 μm sieves. The synthesis of Fe_3O_4 used co-precipitation methods. First, $FeCl_3 \cdot 6H_2O$ and $FeSO_4 \cdot 7H_2O$ with a ratio of 1:2 M in 100 mL solution were mechanically stirred (Velp JL T6) at 600 rpm. Then, 10 mL NH_4OH solution and 2 g of MMT were mixed in a 250 mL flask at 30 °C. The solution containing $FeCl_3 \cdot 6H_2O$ and $FeSO_4 \cdot 7H_2O$ was slowly added and mixed in a mechanical stirrer at 30 °C for 3 h. The precipitated black colored nanoparticles were separated from the solution and washed several times to ensure the pH of the suspension was 7 and then dried in an oven at 60 °C

for 24 h. Particles were sieved with 250 μm sieves and stored in a desiccator to be used as Fe_3O_4/MMT catalyst. The utilized MMT samples for catalyst production and produced magnetic nanoscale catalyst images are shown in Figure 1. A possible mechanism for synthesis is shown by Eq. 5 [22,23].



RO16 dye was commercially purchased from Sigma Aldrich ($\geq 70\%$ purity) (Cas No: 12225-83-1). The RO16 solution was prepared with distilled water and used at a constant concentration of 100 mg/L to better understand the effect of other system parameters on the heterogeneous Fenton process. The physical and chemical properties of RO16 are given in Table 1.

Table 1. Properties of RO16.

Type of Dye	Anionic
Chemical Formula	$C_{20}H_{17}N_3Na_2O_{11}S_3$
Soluble	Water
Melting Point	>300° C
Appearance	Powder

Analytical methods and calculations

All experiments were carried out in 250 mL flasks with 100 mL dye solution volume using an orbital shaker. In this study, two types of experiments were conducted. The first was a control experiment in which the efficiency of H₂O₂ oxidation, adsorption, and heterogeneous Fenton processes on COD removal efficiency was determined. The second is the heterogeneous Fenton process with the optimization procedure. Both experimental procedures are as follows; first, dye solutions at the desired concentration were put into flasks, then the desired amount of catalyst was added and mixed at 150 rpm for 30 min at room temperature to establish adsorption/desorption equilibrium. After equilibration, the pH values of the solutions were adjusted as desired, and the heterogeneous Fenton reaction was recorded after adding H₂O₂ at the desired concentration. 5 mL samples were withdrawn at the specified time intervals and then transferred to tubes containing 10 µL of 2M Na₂SO₃ solution by filtration with a 0.45 µm syringe filter. The Na₂SO₃ solution was used to quench the excess H₂O₂ [24]. The degree of degradation of RO16 in each solution was measured according to the closed reflux colorimetric method [25] as COD removal (%). The release of iron from magnetic nanoscale catalysts into solution was investigated with the help of atomic absorption spectroscopy (AAS) (Thermo Scientific/ICE-3000 series). The presence of H₂O₂ can interfere with COD analysis [26]. For this reason, to calculate the residual H₂O₂ concentration, readings were done according to the methods proposed by Talinli and Anderson [27] and Benatti et al. [28].

For possible adsorption in the syringe filter and the sampling container, the syringe and tube were washed several times with distilled water and analyzed with UV-vis spectrophotometer (WTW6100vis) for RO16 at a wavelength of 494 nm, and results were below the detection limit. The COD removal efficiency was calculated with Eq. 6.

$$\text{Removal efficiency}(\%) = \frac{(C_0 - C_t)}{C_0} \times 100 \quad (6)$$

Where; C₀ refers to the initial COD concentration (mg/L) of RO16, and C_t refers to the COD concentration in the sample taken at time t.

Characterization of catalyst

The morphological, chemical composition and crystal structure of the synthesized catalyst were determined by scanning electron microscope (SEM), energy-dispersive X-ray spectroscopy (EDX) (Zeiss Sigma 300, EDAX-Metek), transmission electron microscopy (TEM) (Hitachi HighTech HT7700), and X-ray diffraction (XRD) analysis (PANalytical Empyrean XRD), respectively. Surface area-pore size, surface chemistry, and size and distribution of particles were determined by Brunauer-Emmett-Teller (BET) (Micrometrics 3Flex), Fourier transform infrared spectroscopy (FTIR) (Thermo Scientific, Nicolet iS10) and zeta sizer with dynamic light scattering (DLS) (NanoPlus3), respectively.

Optimization pathway

Optimization techniques are applied in many areas such as experimental design, architecture, etc. Optimization can simply be defined as ‘making the best decisions for a situation in the most economical way’. Optimization techniques are possible today in many ways, such as statistical-mathematically based programs, artificial intelligence modelling, machine learning, etc. Of course, applying optimization models is not the only way to make the best decisions about an experimental system; however, it may be necessary to ‘optimize’ one of the system’s parameters while keeping the others constant in traditional methods. This situation may cause excessive experimentation, labour, chemical consumption, and time loss for systems that contain many parameters due to their nature. In addition to being economical compared to traditional methods, response surface methodology (RSM) is based on the essential point of ‘fewer experiments - more data’ to reveal the effects of variables on system outcomes. RSM is a statistical-mathematical tool that contains more than one optimization model. Still, it is mainly used to determine the effects of multiple system parameters on one and/or more system outputs, investigate the experimental space of independent parameters, and optimize systems [4]. Central Composite Design (CCD) is one of the optimization models within RSM. It is a design useful in the surface methodology of the response to generate a quadratic model for the CCD system output. However, the response can be associated with system inputs by linear or quadratic models. A quadratic model can be expressed by Eq. 7.

$$\hat{y}_n = \beta_0 + \sum_{i=1}^n \beta_i x_i + \sum_{i=1}^n \beta_{ii} x_i^2 + \sum_{i=1}^n \sum_{j=i+1}^n \beta_{ij} x_i x_j + \varepsilon \quad (7)$$

β_0 is the constant dependent variable at the centre of the model design, and linear, quadratic, and interactive effects of regression expressions are represented by β_i , β_{ii} , and β_{ij} , respectively. n represents the independent variables in the system, ϵ the random error and X_i stands for the level of the independent parameters.

CCD is a two-level factorial design that includes repetitive points that play a key role in many areas, such as the experimental error in the centre of the system's design, the system's self-repeatability, etc. The system inputs and outputs refer to the parameters that affect the system (independent variables) and response (dependent variable), respectively. In this study, catalyst dos-

age, H_2O_2 concentration, reaction time, and solution pH were determined to be independent system variables, and COD removal (dependent variable) was selected as an expression of system efficiency. The max. (+1) & min. (-1) values of the system input parameters defined in the model and the centre (0) values determined by the system are shown in Table 2. A total of 30 experiments were proposed by the program (Design Expert 12) according to Eq. 8, where; k is the independent parameter number (4 in this study), and 6 is repetitive points in the design centre.

$$2^k + 2k + 6 \quad (8)$$

Table 2. Levels of independent parameter values for CCD experiments.

Parameters	Min.	Center	Max.
Catalyst Dosage (g/L)	0.5	1.75	3
H_2O_2 Concentration (mM)	15	82.5	150
Solution pH	2	3	4
Reaction time (min)	10	37.5	60

pH has a very decisive role in Fenton processes. For this reason, the maximum and minimum values of the pH parameter to be defined in the CCD model were determined with a few preliminary trials to prevent the possibility of moving away from the optimum point. As a result of the experiments, a value of 2-4 was chosen (Table 2), which is thought to be in the closest range to the optimum response due to the decrease in system efficiency at values above pH 4.

RESULTS and DISCUSSION

Characterization of catalyst

The prepared samples' phase structure and bond types were characterized by XRD and FTIR analysis, respectively. The data from XRD and FTIR analysis of Fe_3O_4 /MMT are shown in Figure 2(a) and (b), respectively. As can be seen from the XRD pattern (Figure 2(a)), reflections at $2\theta = 19.79^\circ$, 20.84° , 26.65° , and 50.07° correspond to MMT and reflections observed at $2\theta = 35.58^\circ$, 30.46° , 57.58° , and 63.12° belong to the Fe_3O_4 structure. The data from XRD are in good agreement with the Powder Diffraction Standards Joint Committee (JCPDS) database (file no: 01-088-0315). This can be regarded as an indication that Fe_3O_4 was successfully emplaced on MMT. XRD analysis of local MMT was made to bet-

ter understand Fe_3O_4 dispersion on the surface/interface of local MMT after catalyst synthesis. According to XRD results for local MMT taken from the Horasan region, the basal spacing value was 1.53 nm ($2\theta = 5.78^\circ$). But for Fe_3O_4 /MMT, this value ($2\theta = 8.95^\circ$) changed to 0.99 nm in this study. This situation may indicate that the Fe_3O_4 particles are dispersed on the surface of the MMT instead of the intermediate layers [29]. Based on the reports of Lee and Tiwari (2012) [30] and Chang et al. (2016)[29], they attributed a similar situation to the replacement of Ca and Mg ions in the structure of MMT with hydrogen ions added to the silicate layers and the loss of water in these intermediate layers during synthesis. According to this result, it can be concluded that there is a tightening in the interlayer space of MMT, and Fe_3O_4 nanoparticles were successfully incorporated into the structure of MMT. The presence of Fe_3O_4 diffraction scattering confirms the existence of Fe_3O_4 on the surface of MMT. It can be said that Fe_3O_4 /MMT nanoparticles successfully reflect the crystal properties of both Fe_3O_4 and MMT in a single structure.

FTIR spectra for Fe_3O_4 and Fe_3O_4 /MMT are shown in Figure 2(b). The 3694 cm^{-1} and 3622 cm^{-1} peaks observed in the FTIR spectrum correspond to the stretching vibration of the -OH groups in the structure of MMT [31,32]. It can also be said that these bands, which are

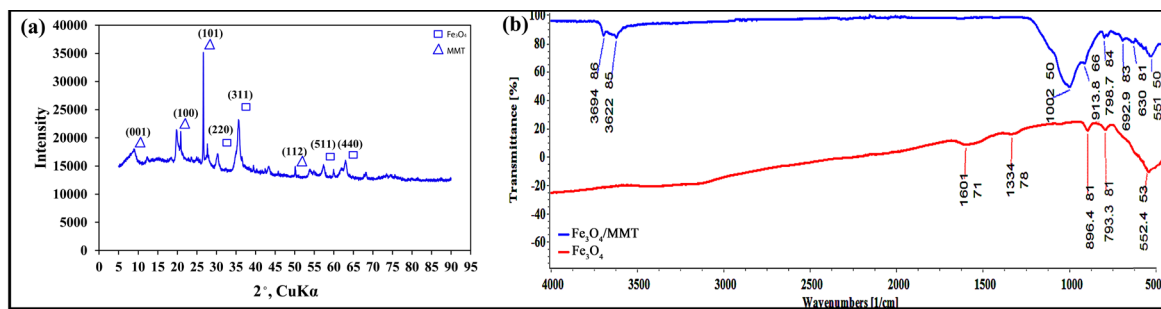


Figure 2. (a) Size distribution and (b) Zeta potential of Fe₃O₄/MMT.

not observed in Fe₃O₄, are caused by water molecules. The broad bands observed at 1002.50 cm⁻¹ and 693 cm⁻¹ can be attributed to the Si–O–Si stretching vibrations caused by MMT. While 913.8 cm⁻¹ corresponds to the Al–OH deformation, 798.7 cm⁻¹ may result from Si–O stretching vibrations [33]. The peaks observed at 630.81 cm⁻¹ and 551.50 cm⁻¹ can be attributed to Fe–O vibrations [34], which indicates that the addition of Fe₃O₄ to MMT was successful. Bands at 896.4 cm⁻¹ and 793.3 cm⁻¹ in the Fe₃O₄/MMT FTIR spectrum can be attributed to Fe–O–H bending vibrations. The band at 551.50 cm⁻¹ in the pure Fe₃O₄ spectrum corresponds to Fe–O vibrations [34]. The observed peaks at 1601.71 cm⁻¹ and 1334.78 cm⁻¹ show the presence of H₂O molecules [35]. According to results from FTIR spectra, Fe₃O₄/MMT has both MMT, and Fe₃O₄ crystallographic features and synthesis of Fe₃O₄/MMT was achieved successfully.

The surface morphology and elemental compositions of Fe₃O₄/MMT samples were determined with SEM/EDX analysis, and the results are shown in Figure 3. As can be seen from Figure 3(a), Fe₃O₄ nanoparticles have inhomogeneous distribution in size on MMT due to the magnetic interaction between particles. The Fe₃O₄ nanoparticles are mostly dispersed on the MMT surface with some agglomeration clusters. However, this does not mean that Fe₃O₄ particles are not dispersed within the interlayers of MMT. When the left side of Figure 3(a) is examined, Fe₃O₄ nanoparticles are dispersed among the flake structures. However, this dispersion may not have occurred sufficiently between all the flakes of MMT for detection with XRD analyses. It is noteworthy that the Fe₃O₄ nanoparticles formed a cauliflower-like structure, and they agglomerate in some places. These results are in good agreement with the literature [36,37]. Individual particles are spherical, which supports the crystallographic data observed in the XRD pattern. The dispersion of Fe₃O₄ nanoparticles with an average sphere diameter of about 20.67 nm on the mud

crack-like structures of MMT is obvious.

As can be seen from Figure 3(b), the expected elements of MMT and Fe₃O₄ are obtained on the EDX graph. While high rates of Si and O are the major elements in MMT, Fe comes from Fe₃O₄. According to the EDX graph, Fe₃O₄ nanoparticles were successfully added to the MMT structure.

TEM images of Fe₃O₄/MMT at 100 nm (right) and 200 nm (left) magnitudes are shown in Figure 4. The TEM images show that the individual particles are distributed with sizes between 20 nm and 40 nm, and they are mostly spherical. On the other hand, these particles are agglomerated with a wide variety of sizes due to magnetic interaction. It is clear that the Fe₃O₄ nanoparticles were successfully dispersed into and/or onto the MMT layers and these results are in good agreement with the SEM images.

To obtain clearer information about the particle polydispersity index (PDI) and the size of the particles, DLS analysis was completed (Figure 5). Also, zeta potential analysis was conducted to identify the surface charge. As shown in Figure 5(b), the zeta potential of the catalyst was -21.46±1.4 mV as the average of 3 repeated readings. The negative zeta potential value indicates that Fe₃O₄/MMT particles have good stability and dispersion [38]. Depending on the negative value, less agglomeration is expected as a result of the nanoparticles pushing each other on the negatively charged surface. The mechanisms in the aggregation are van der Waals forces and the chemical structure of the particles [39–41].

Additionally, the mobility value of Fe₃O₄/MMT particles was determined as -1.674e-004 cm²/Vs. As can be seen from Figure 5 (a), the particle size distribution is generally concentrated in three ranges. Fe₃O₄/MMT particles were distributed in approximately 1-7 nm, 27-47 nm, and 67-97 nm. Particles observed with sizes 1-7

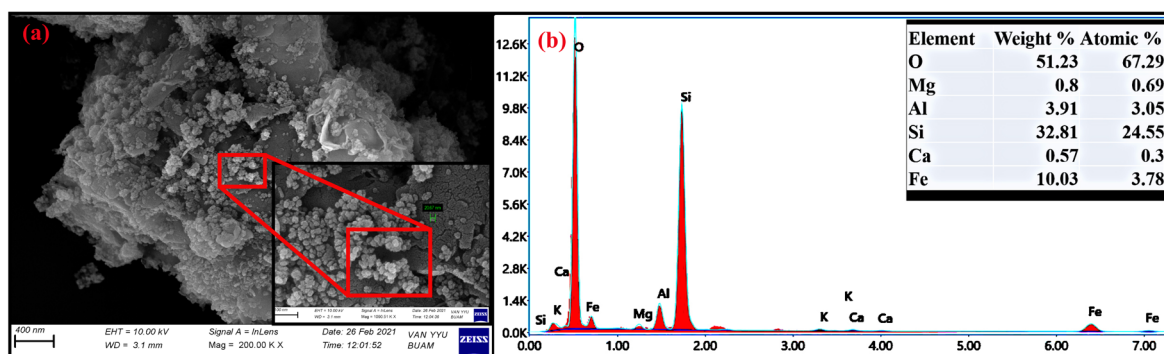


Figure 3. SEM images and EDX analysis of $\text{Fe}_3\text{O}_4/\text{MMT}$.

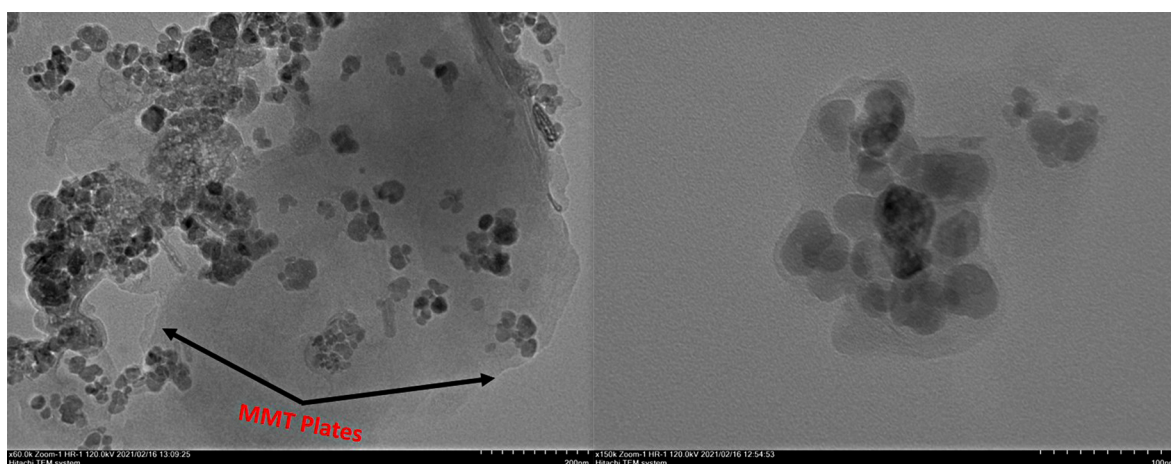


Figure 4. TEM images of $\text{Fe}_3\text{O}_4/\text{MMT}$ particles.

and 27-47 nm can be attributed to the size of individual particles, as can be confirmed from the TEM and SEM images. The dispersion in the range of 67-97 nm can be attributed to aggregated particles formed by the combination of small particles. In addition, some large-sized individual particles that were not aggregated, even in small amounts, were distributed in this range. DLS results are in good agreement with SEM and TEM analyses. The dimensionless PDI assessment, known as the heterogeneity index, is important to better define the particle size distribution [42]. PDI values lower than 0.5 indicate that the particles are monodispersed, while values greater than 0.5 indicate that the particles are polydispersed [43]. In this study, PDI values were found to be 0.53. Therefore, it can be said that $\text{Fe}_3\text{O}_4/\text{MMT}$ particles are polydispersive in size. These results highlight the difficulty of homogeneously distributed/size-controlled particle synthesis [44] despite applying a careful synthesis procedure.

According to the results of the BET analysis, the surface area of $\text{Fe}_3\text{O}_4/\text{MMT}$ nanoparticles and local MMT was

determined as $40.0431 \text{ m}^2/\text{g}$ and $49.1387 \text{ m}^2/\text{g}$, respectively. The reduced surface area may be a sign of Fe_3O_4 nanoparticles being successfully doped into the surface and/or interface of the MMT. Fe_3O_4 added to the open pores of local MMT on the surface structures may have caused a decrease in the surface area. Similarly, Ain et al. [45] reported that the surface area of pure bentonite, which was $55.62 \text{ m}^2/\text{g}$, decreased to $27.49 \text{ m}^2/\text{g}$ for Fe_3O_4 -PDA-bentonite after synthesis. They attributed this decrease to Fe_3O_4 accumulation in the mesopores of bentonite.

Investigation of catalyst activity

In the study, $\text{Fe}_3\text{O}_4/\text{MMT}$ samples used as an iron source were investigated to contribute to the heterogeneous Fenton process during the adsorption process due to their large surface area. For this purpose, trials including only H_2O_2 , only $\text{Fe}_3\text{O}_4/\text{MMT}$ catalyst, and H_2O_2 and $\text{Fe}_3\text{O}_4/\text{MMT}$ were carried out. The efficiency of the processes was investigated at different time intervals (5-60 min) according to COD removal (%). All three trials were conducted at constant 50 mg/L dye concentra-

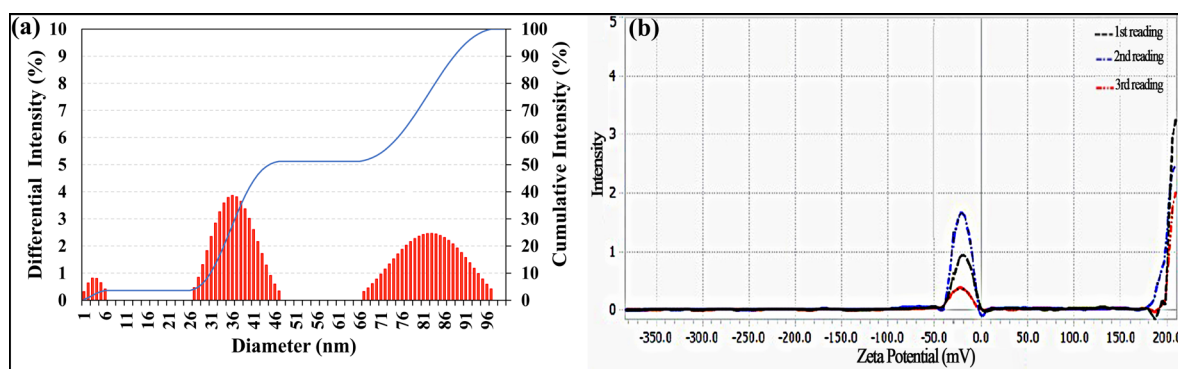


Figure 5. (a) Zeta potential and (b) size distribution of Fe₃O₄/MMT.

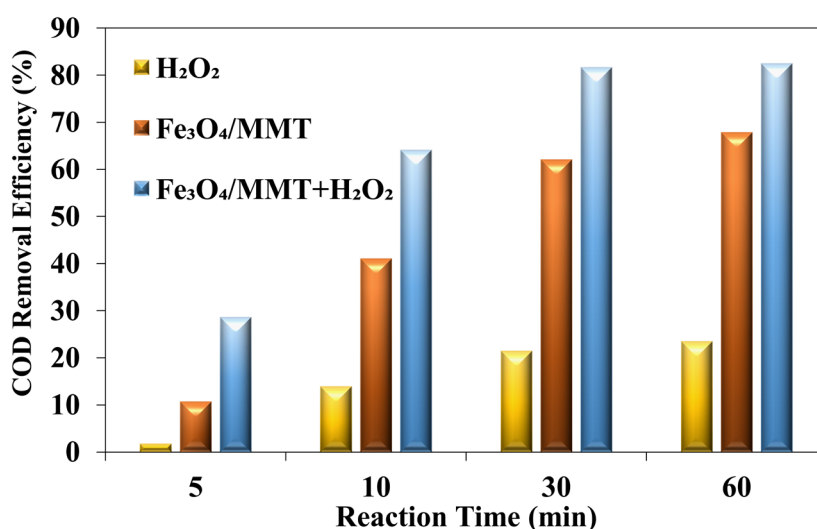


Figure 6. Effect of processes on COD removal.

tion, 150 rpm constant agitation speed, and initial pH of 3. In the trials where the catalyst was used, the dose was kept constant as 1.5 g/L, and in the trials where H₂O₂ was used, the concentration was kept constant as 50 mM. COD removal efficiencies were determined as a function of time at 5, 10, 30, and 60 minutes. Results are shown in Figure 6.

As shown in Figure 6, components of the heterogeneous Fenton process affected the efficiency of COD removal in the order of H₂O₂ oxidation < adsorption < heterogeneous Fenton process. H₂O₂ oxidation alone has a maximum capacity of 23.56% to degrade RO16, the adsorption process had a maximum of 67.92%, and the heterogeneous Fenton process had a maximum of 82.54%. Low COD removal efficiencies with H₂O₂ can be attributed to the low oxidation potential of H₂O₂ in the absence of the catalyst. Similar situations were reported in the literature [46–48]. The reason for the high COD removal

efficiency observed for the adsorption process can be related to the high surface area of Fe₃O₄/MMT, ambient pH, and pH_{pzc} of Fe₃O₄/MMT. The pH_{pzc} value of Fe₃O₄/MMT used in this study was determined to be 5.8 according to the drift method [49] to interpret better the adsorption process's efficacy in the heterogeneous Fenton process. Simply, pH_{pzc} describes the pH value of the adsorbent at which the electrical surface charge is zero. The adsorption of positively charged ions at pH values above pH_{pzc} and negatively charged ions at pH values lower than pH_{pzc} is advantageous [1]. Therefore, the initial pH value of the wastewater, which is kept constant under the conditions of control trials, was lower than the pH_{pzc} value of Fe₃O₄/MMT; in this case, the surface of Fe₃O₄/MMT may have been protonated, enabling the negatively-charged RO16 dye molecules to be adsorbed by electrostatic attraction. Also, clay group minerals such as MMTs have a high surface area. The BET surface area of Fe₃O₄/MMT used in this study

Table 3. ANOVA for Quadratic model.

Source	Sum of Squares.	df	Mean Square	F-value	p-value	
Model	13433.80	14	959.56	711.70	< 0.0001	significant
A-Catalyst Dosage	101.48	1	101.48	75.27	< 0.0001	
B-H ₂ O ₂ Concentration	5.04	1	5.04	3.73	0.0724	
C- pH	418.76	1	418.76	310.59	< 0.0001	
D-Reaction time	189.41	1	189.41	140.49	< 0.0001	
AB	12.02	1	12.02	8.92	0.0092	
AC	7.74	1	7.74	5.74	0.0300	
AD	0.9653	1	0.9653	0.7160	0.4108	
BC	52.89	1	52.89	39.23	< 0.0001	
BD	49.60	1	49.60	36.79	< 0.0001	
CD	33.44	1	33.44	24.80	0.0002	
A ²	1349.62	1	1349.62	1001.00	< 0.0001	
B ²	227.15	1	227.15	168.48	< 0.0001	
C ²	635.65	1	635.65	471.46	< 0.0001	
D ²	12.33	1	12.33	9.15	0.0085	
Residual	20.22	15	1.35			
Lack of Fit	14.50	10	1.45	1.27	0.4197	not significant
Pure Error	5.73	5	1.15			
Cor Total	13454.02	29				
R ²	0.9985					
Adjusted R ²	0.9971					
Predicted R ²	0.9931					
Adeq Precision	81.6199					

was determined (Micromeritics - 3Flex) as 40.0431 m²/g, so it can be said that this situation provided an advantage for the adsorption of RO16 molecules. In COD removal, Fe₃O₄/MMT reached an efficiency of approximately 41% in the first 10 minutes and stabilized with 62% efficiency up to the 30th minute, and the efficiency remained at 67% in the 60th minute. Although the Fe₃O₄/MMT catalyst has good adsorptive property, the efficiency of the heterogeneous Fenton process is higher than adsorption at all time intervals when COD removal efficiency analysis is examined. Therefore, it can be concluded that the adsorption process is effective in COD removal, but heterogeneous Fenton is the more dominant process.

In order to verify the degradation of RO16 by the heterogeneous Fenton process, FTIR analysis of the catalyst was investigated after the reaction (Figure 7). It is clear from Figure 7 that the signature peak observed at 1635.84 cm⁻¹ may correspond to N=N stretching vibration. A similar interpretation for the peak observed at 1635 cm⁻¹ was made by Chittal et al. [50], in which they

dealt with the degradation of RO16, and they attributed this reflection to the azo group in RO16. After the heterogeneous Fenton process, another new peak in the catalyst was observed at 1116.99 cm⁻¹. This new peak can be attributed to C-H bending vibrations. Telke et al. [51] stated that the peaks observed at 1103.96 cm⁻¹, 1302.68 cm⁻¹, 1453.93 cm⁻¹, 1660 cm⁻¹, and 2959.32 cm⁻¹ after degradation of RO16 can be attributed to 6-nitro naphthol and dihydroperoxy benzene, which are the final products of RO16. The broad new peak observed at 3427 cm⁻¹ may indicate N-H stretching vibrations. All new peaks observed confirmed the degradation of RO16.

Analyses of the established model, experimental matrix, and effects of independent parameters

ANOVA is a technique that helps to determine the effect of the variation in independent parameters affecting the system on dependent parameters. Usually, ANOVA tests are applied by comparing the intergroup variance to the in-group variance [52]. Also, it is possible to obtain information about the significance of independent

factors and analyze the equality of means statistically with the F-test and the ANOVA test. The results of the ANOVA test are shown in Table 3. The p-value in the ANOVA test can be used to obtain information about the extent to which the individual, interaction, and quadratic effects of independent parameters change the response. A, B, C, and D represent the individual effects of independent parameters, AB, AC, AD, BC, BD, and CD represent the interaction effects, and A^2 , B^2 , C^2 and D^2 represent the quadratic effects. P-values less than 0.05 indicate model terms are significant. In this case, A, C, D, AB, AC, BC, BD, CD, A^2 , B^2 , C^2 , and D^2 are significant model terms. Values greater than 0.1 indicate the model terms are not significant. In this study, catalyst dose, H_2O_2 concentration, pH, and reaction time were selected as independent parameters, which are reported to be significant operating parameters for heterogeneous Fenton processes in the literature [53,54]. However, the extent to which these independent parameters affect the system differs in each study. As mentioned above, Table 3 shows that a one-unit change in catalyst dosage, reaction time, and pH affects COD removal efficiency by 99.99% ($p < 0.0001$), while a one-unit change in H_2O_2 concentration affects COD removal efficiency by 92.76% ($p: 0.0724$). Also, the significance of each term is expressed in a quadratic model by the value of F. From the ANOVA test, the F value of the established model is 711.70, and the p-value is < 0.0001 . These results imply that the model is significant, and there is only a 0.01% chance that an F-value this large could occur due to noise.

CCD is generally useful in cases where the experimenter has insight/experience about the parameters affecting the system (to keep the number of experiments low). However, in cases where the experimenter has no prediction/idea or experience about the parameters that may affect the system, it is possible to determine the most effective parameters with the help of designs

such as Plackett Burman Design (PBD) [55], Fractional Factorial Design (FFD) [56], etc. In this study, the parameters that were thought to affect the system most were evaluated in line with the preliminary trials, similar studies in the literature, and experience. The ANOVA test confirmed that the chosen parameters have high significance for the response.

The lack of fit value is generally used to measure the model adequacy. So, according to Table 3, the lack of fit F-value is 1.27, and this implies the lack of fit is not significant relative to the pure error. Based on the low lack of fit value, the model is valid and logical. The model accurately predicts any combination of independent parameters at the studied levels [4].

Another statistical parameter is R^2 , and it is a measure of how well the regression approaches the actual values. Thanks to this data, comments can be made about the compatibility of the model. As can be seen from Table 3, the regression coefficient of the model was 0.9985, so 99.85% of the variation in the response can be successfully predicted by the second-order model, and 0.15% is due to residues [57]. As seen from Table 3, the predicted R^2 of 0.9931 is in reasonable agreement with the adjusted R^2 of 0.9971; i.e. the difference is less than 0.2. Adequate precision measures the signal-to-noise ratio. A ratio greater than 4 is desirable. The ratio of 81.620 indicates an adequate signal. So, the established model can be used to navigate the design space. Similar comments were made in the literature [58,59]. As a result, it can be concluded that the model established with a small p-value, large F-value, and high R^2 value meets the best regression model criteria.

The experimental matrix proposed by the CCD program and the results of the experiment sets are shown in Table 5. The non-coded model equation based on the

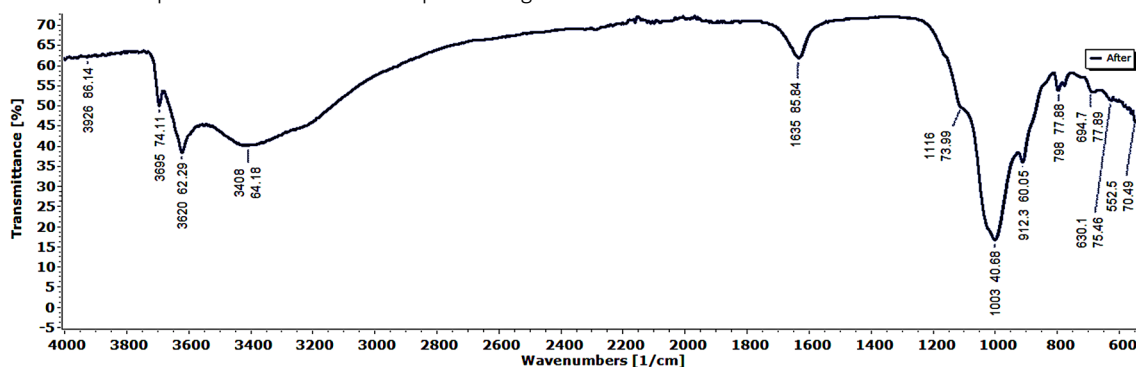


Figure 7. FTIR spectra of Fe_3O_4 /MMT after heterogeneous Fenton process.

Table 4. Experimental matrix and results.

Run	A C. Dosage (g/L)	B H ₂ O ₂ Conc. (mM)	C pH	D R.time (min)	Actual value (observed COD removal %)	Predicted value y _p	Corresponded Error (y _o -y _p)
1	0.5	150	4	60	33.61	33.00	0.61
2	1.75	82.5	4	37.5	59.26	58.78	0.48
3	0.5	150	4	15	26.64	27.63	-0.99
4	1.75	15	3	37.5	69.17	69.38	-0.21
5	0.5	150	2	60	34.84	34.72	0.12
6	0.5	82.5	3	37.5	53.15	54.07	-0.92
7	0.5	15	4	60	30.01	30.09	-0.08
8	3	15	4	60	35.04	35.67	-0.63
9	1.75	150	3	37.5	69.84	70.44	-0.6
10	1.75	82.5	3	37.5	79.77	79.27	0.5
11	1.75	82.5	3	37.5	81.06	79.27	1.79
12	1.75	82.5	3	15	76.54	78.21	-1.67
13	3	82.5	3	37.5	58.94	58.82	0.12
14	1.75	82.5	3	37.5	78.25	79.27	-1.02
15	1.75	82.5	3	60	85.56	84.70	0.86
16	3	150	4	15	29.77	28.76	1.01
17	3	150	4	60	34.34	35.11	-0.77
18	1.75	82.5	3	37.5	80.03	79.27	0.76
19	0.5	15	4	15	18.16	17.68	0.48
20	3	15	4	15	22.18	22.28	-0.1
21	1.75	82.5	3	37.5	78.58	79.27	-0.69
22	1.75	82.5	3	37.5	80.34	79.27	1.07
23	1.75	82.5	2	37.5	67.15	68.43	-1.28
24	3	150	2	15	39.15	39.06	0.09
25	0.5	15	2	60	38.27	39.09	-0.82
26	0.5	150	2	15	35.96	35.14	0.82
27	3	15	2	15	39.42	39.85	-0.43
28	0.5	15	2	15	33.25	32.46	0.79
29	3	150	2	60	39.33	39.62	-0.29
30	3	15	2	60	48.46	47.46	1

independent parameters that affect the COD removal efficiency is shown in Eq. 9. The equation in terms of uncoded factors can be used to make predictions about the response for given levels of each factor. The validity of a model can also be interpreted in terms of how well it can predict real values within specified limits in the established space. It is obvious from Table 4 that for each experimental set, the predicted value is close to the actual value. So, this indicates that the model successfully reflects the experimental results.

$$\begin{aligned}
 \text{COD Removal (\%)} = & -102.792 + 55.2134[\text{C.Dosage}] \\
 & + 0.327565[\text{H}_2\text{O}_2 \text{ Conc.}] + 85.499[\text{pH}] - 0.291431[\text{R.} \\
 & \text{time}] - 0.0102741[\text{C.Dosage}][\text{H}_2\text{O}_2 \text{ Conc.}] - 0.5565[\text{C.} \\
 & \text{Dosage}][\text{pH}] + 0.00873333 [\text{C.Dosage}][\text{R. time}] + \\
 & 0.0269352[\text{H}_2\text{O}_2 \text{ Conc.}][\text{pH}] - 0.00115926[\text{H}_2\text{O}_2 \text{ Conc.}] \\
 & [\text{R. time}] + 0.06425[\text{pH}][\text{R. time}] - 14.6069[\text{C.Dosage}^2] \\
 & - 0.00205505[\text{H}_2\text{O}_2 \text{ Conc.}^2] - 15.6633[\text{pH}^2] + \\
 & 0.00430947[\text{R. time}^2] \quad \quad \quad \text{(9)}
 \end{aligned}$$

The equation in terms of coded factors can be used to make predictions about the response for given levels

Table 5. Coefficients in Terms of Coded Factors.

Factor	Coefficient Estimate	df	Standard Error	95% CI Low	95% CI High	VIF
Intercept	79.27	1	0.3607	78.50	80.04	
A-Catalyst Dosage	2.37	1	0.2737	1.79	2.96	1.0000
B-H ₂ O ₂ Concentration	0.5289	1	0.2737	-0.0545	1.11	1.0000
C-Solution pH	-4.82	1	0.2737	-5.41	-4.24	1.0000
D-Reaction time	3.24	1	0.2737	2.66	3.83	1.0000
AB	-0.8669	1	0.2903	-1.49	-0.2481	1.0000
AC	-0.6956	1	0.2903	-1.31	-0.0769	1.0000
AD	0.2456	1	0.2903	-0.3731	0.8644	1.0000
BC	1.82	1	0.2903	1.20	2.44	1.0000
BD	-1.76	1	0.2903	-2.38	-1.14	1.0000
CD	1.45	1	0.2903	0.8269	2.06	1.0000
A ²	-22.82	1	0.7214	-24.36	-21.29	2.78
B ²	-9.36	1	0.7214	-10.90	-7.83	2.78
C ²	-15.66	1	0.7214	-17.20	-14.13	2.78
D ²	2.18	1	0.7214	0.6441	3.72	2.78

of each factor. By default, high levels of the factors are coded as +1, and low levels are coded as -1. The coded equation is useful for identifying the relative impact of the factors by comparing the factor coefficients. Table 5 shows the coefficients in terms of coded factors.

The coefficient estimate represents the expected change in response per unit change in factor value when all remaining factors are kept constant. The intercept in an orthogonal design is the overall average response of all runs. The coefficients are adjustments around that average based on the factor settings. The variance inflation factor (VIF) is data that helps to interpret the severity of multicollinearity [60]. When the factors are orthogonal, the variance inflation factor (VIF) is 1; VIF greater than 1 indicates multicollinearity and the higher the VIF, the more severe the correlation of factors. According to data from Table 4, linear and interaction of regressors show there is no multicollinearity, but quadratic regressors may be moderately correlated, and the modelling results will be accurately estimated. Akinwande et al. [60] commented that a VIF between 5 and 10 shows a high correlation that could be problematic. If the VIF rises above 10 the regression coefficients could be poorly predicted due to multicollinearity that must be addressed accordingly.

One way to test the established model's satisfaction is with the relationship between predicted values and externally studentized residual values (Figure 8(a)). The proximity of the distribution of colored boxes representing COD removal to the zero axes indicates that there is no constant error [61]. Values distributed over a fixed range close to the zero axis indicate that no clear model confirms the initial constant assumption of variance [62]. In addition, values ranging from +3 to -3 are within acceptable limits. As a result, the established model performs well in predicting COD removal representing RO16 degradation, and there is no reason to suspect any inconsistency. Box-Cox analysis can be used for further evaluation of the statistical adequacy of the results [61] (Figure 8(b)). The current lambda (1) and best lambda (0.81) values are close to each other, indicating that the experimental results best fit the model. Also, the maximum confidence interval value is 1.03, and the minimum value is 0.59. Consequently, power conversion of the model was not required, as suggested by the Box-Cox analysis.

Dual combination effects on H₂O₂ concentration, catalyst dosage, pH, and reaction time response surface were investigated by 3D graphics (Figure 8). Figure 8(c) displays the combined effect of H₂O₂ concentration and catalyst dosage on COD removal. When the reaction time was 37.5 min, pH was 3, and the catalyst dosage

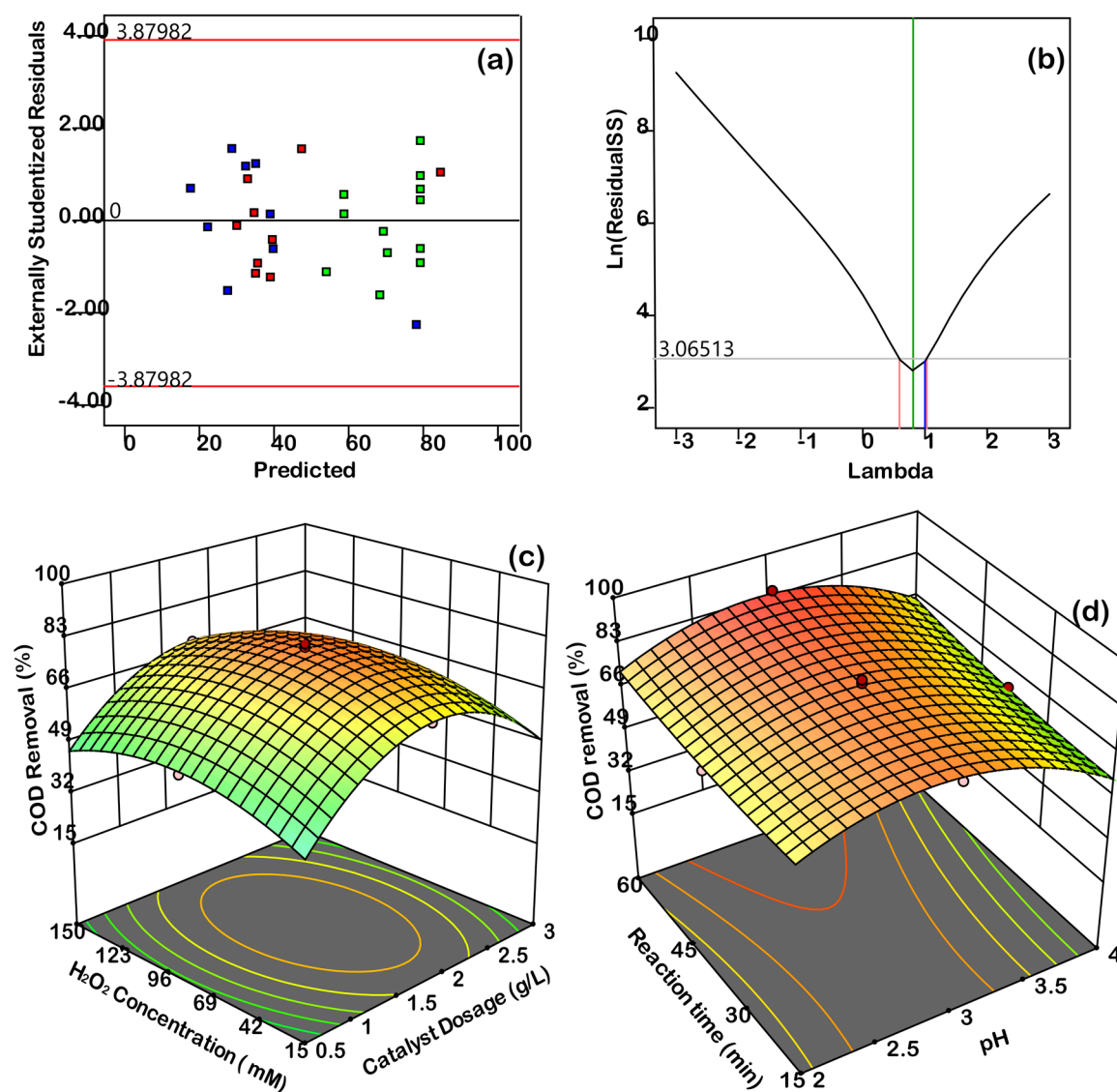
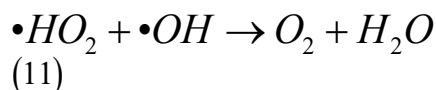
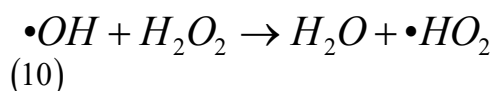
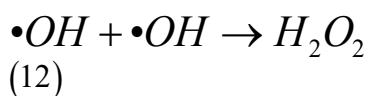


Figure 8. Graph of predicted values vs externally studentized residuals (a) Box-Cox Plot for Power Transforms (b), Combined effects of H_2O_2 and catalyst dosage (c) pH and Reaction time (d) on COD removal.

was constant at 1.75g/L. When the H_2O_2 concentration increases from 15 mM to 82.5 mM, COD removal changed from approximately 69% to approximately 80%. However, above 82.5 mM (at 150 mM), COD removal efficiency decreased to 69% again. Increasing COD removal efficiency with increasing H_2O_2 (up to 82 mM) can be explained by the increased amount of $\bullet OH$ forming. This means more $\bullet OH$ is present to oxidize organic dye molecules (Eq. 1). Decreases in COD removal efficiency with increasing H_2O_2 concentration can be attributed to the formation of $\bullet HO_2$, which has low oxidative potential compared to $\bullet OH$. The excess H_2O_2 acts as a scavenger to consume $\bullet OH$ (Eqs.10 and 11) [63]. An-

other explanation was made by Mashayekh-Salehi et al. [64] for decreasing removal efficiency with increasing H_2O_2 . They stated that the $\bullet OH$ recombined to generate H_2O_2 (Eq. 12) [65,66]. According to the results, H_2O_2 acts both as an $\bullet OH$ promoter and scavenger related to the concentration.





When the reaction time was 37.5 min, pH was 3, and the H_2O_2 concentration was 82.5 mM, when the catalyst dose increased from 0.5 g/L to 1.75 g/L, the COD removal efficiency reached approximately 80%, and the removal efficiency decreased at catalyst doses higher than this value. It decreased to approximately 58% at 3 g/L. Increasing catalyst dosage leads to an increase in removal efficiency due to the increase in the active adsorption sites in Fe_3O_4 /MMT and the increased catalytic sites. Although the contribution of the adsorption process is slower and less effective than the heterogeneous Fenton process (see section), this does not mean that the adsorption process cannot contribute to removal efficiency with the increase of catalyst dose, contrarily it leads to enhanced adsorption of RO16. Similar comment was made by Sétifi et al. [67]. At the same time, the degradation efficiency of RO16 increased due to the increase in Fe-rich active sites in an aqueous environment with increasing catalyst dosage. So, this leads to more generation of $\bullet OH$, resulting in more oxidation of dye molecules. The reduced COD removal efficiency observed at higher doses can be attributed to the self-scavenging effect of the excess hydroxyl radicals with Fe ions (Eq. 13) [68,69]. Another reason may be the agglomeration of the particles using high doses of Fe_3O_4 /MMT. The reactive area of the catalyst decreases due to agglomeration, resulting in less Fe being added to the oxidation reaction. Similar comments are found in the literature [70,71].

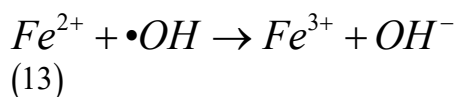
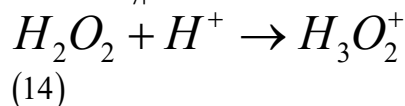


Figure 8(d) reveals the combined effect of pH and reaction time on COD removal efficiency. While the catalyst dose was constant at 1.75 g/L, H_2O_2 concentration was

82.5 mM, the highest COD removal efficiency was observed at pH 3 (85%) when the reaction time was 60 min. It is clear from Figure 8(d) that when the reaction time was 37.5 min, the removal efficiency at pH 2 was about 67%, while the removal efficiency dropped to about 59% at pH 4. The hydrogen ion, which is present in high amounts in an aqueous environment at highly acidic conditions, reacts with hydrogen peroxide to form hydroxyoxidanium ions (Eq. 14) [72]. This ion enhances the stability of hydrogen peroxide and limits the hydroxyl radicals, causing a decrease in COD removal efficiency [72]. The low COD removal efficiency observed at pH higher than 3 may be due to both the rapid decomposition of H_2O_2 into H_2O and O_2 under these conditions [73] and the formation of iron hydroxide complexes. As a result, a decrease in COD removal efficiency was observed with the formation of less powerful oxidant types.



It is clear from Figure 8(d) that increasing reaction time has a positive effect on COD removal efficiency. While the catalyst dose was constant at 1.75 g/L, H_2O_2 concentration was 82.5 mM, pH was 3; when the reaction time increased from 15 minutes to 60 minutes, the COD removal efficiency increased from about 76% to 85%. In short reaction times, as the dye molecules and metabolites could not react with enough oxidant, sufficient degradation might not have occurred, and with the increased reaction time, the dye molecules and metabolites had sufficient opportunity to degrade.

Numerical optimization

Optimizing a system is possible with both classical methods and statistical and mathematical programs. RSM enables the optimization of a system both graphically and numerically. Numerical optimization is a technique based on predicting the response when the experimenter limits the system input and output parameters within the desired range or target. From the options offered by the system for numerical optimization, choices should be selected based on low cost and high efficiency. If the selection suggested by the system has at least 0.99 of 'desirability' value, it increases the system predictability of response. Limitations for

Table 6. Numerical optimization constraints.

Parameter	Goal	Lower Limit	Upper Limit
A: Catalyst Dosage	is in range	0.5	3
B: H_2O_2 Conc.	is in range	15	150
C: Solution pH	is target = 3	2	4
D: Reaction time	is in range	15	60
COD removal	maximize	18.16	85.56

the numerical optimization of the system are shown in Table 6. While the independent parameters, except pH, were defined as 'in range', the pH value was determined as the 'target' at pH 3 since maximum COD removal efficiency was observed at this value. In addition, the dependent parameter was 'maximized' to keep the system efficiency high.

Theoretically optimized conditions were determined as catalyst dosage of 1.83 (g/L), H₂O₂ concentration of 77.98 (mM), solution pH of 3, and reaction time of 60 min, and COD removal efficiency was estimated as 84.82% with the desirability of 0.99. To test the model estimation success an experiment was conducted under these conditions, and COD removal efficiency was 85.90%. As seen, the observed and estimated responses were close to each other. So these conditions are optimum for COD removal in this study. Also, the effluent was tested for a possible iron leach by atomic absorption spectrometry (AAS) under optimum conditions, and results showed that leached iron was 0.22 mg/L. This result showed that Fe₃O₄/MMT can be used efficiently and did not lose a high amount of iron leaching in at least one cycle.

Applying limitations as 'minimized' for H₂O₂ concentration and catalyst dose will reduce the cost of the system. Although COD removal efficiency was selected as 'maximize', the estimated maximum removal efficiency among proposed solutions was 72.05%. In addition, the 'desirability' value for this solution was 0.85. This shows that these constraints reduce the predictability of the model. Therefore, these restrictions applied to reduce the system operating cost resulted in lower COD removal efficiency. This shows why both low cost and high efficiency are not possible together in this study. It can be concluded that the synthesized Fe₃O₄/MMT nanocatalyst can be used successfully for the degradation of RO16 dye under optimized conditions with the heterogeneous Fenton process

CONCLUSION

Magnetic Fe₃O₄/MMT nano-sized catalyst reflected both MMT and Fe₃O₄ crystalline structure in XRD analysis, verifying the synthesis process was successful.

The nanoparticles had polydispersive size and good surface area. The catalyst displayed good performance as an iron source for the heterogeneous process and as a potential adsorbent for the adsorption process. The

heterogeneous Fenton process was more dominant and faster than the adsorption process. Degradation metabolites of RO16 were verified by FTIR analysis. CCD was used to optimize independent parameters numerically. The established model is best fitted to the quadratic model. The model was valid and logical and had accurate adequacy to predict any combination of independent parameters at the studied levels. Optimum conditions were determined both experimentally and theoretically as catalyst dosage of 1.83 (g/L), H₂O₂ concentration of 77.98 (mM), solution pH of 3, and reaction time of 60 min. Removal efficiencies for theoretical and experimental were 84.82 and 85.90%, respectively, and leached iron concentration was determined to be 0.22 mg/L. Since MMT is abundant in nature, the synthesis and use of Fe₃O₄/MMT as a heterogeneous Fenton catalyst to degrade organic dyes in aqueous media can be a promising catalyst.

References

1. D. Ozturk, T. Sahan, T. Bayram, A. Erkus, Application of Response Surface Methodology (Rsm) To Optimize the Adsorption Conditions of Cationic Basic Yellow 2 Onto Pumice Samples As a New Adsorbent, *Fresenius Environ. Bull.*, 26 (2017) 3285–3292.
2. T.A. Egerton, H. Purnama, Does hydrogen peroxide really accelerate TiO₂ UV-C photocatalyzed decolouration of azo-dyes such as Reactive Orange 16?, *Dye. Pigment.* (2014).
3. P. Ilgin, Adsorption of Cationic Dye on Anionic Hydrogel and Its Second Use for Drug Delivery with Antibacterial Properties, *Hacettepe J. Biol. Chem.*, 4 (2018) 577–591.
4. D. Ozturk, A.E. Yilmaz, Investigation of electrochemical degradation of Basic Red 13 dye in aqueous solutions based on COD removal: numerical optimization approach, *Int. J. Environ. Sci. Technol.*, 17 (2020) 3099–3110.
5. A. Akhtar, Z. Aslam, A. Asghar, M.M. Bello, A.A.A. Raman, Electrocoagulation of Congo Red dye-containing wastewater: Optimization of operational parameters and process mechanism, *J. Environ. Chem. Eng.*, 8 (2020) 104055.
6. F.M. Gunawan, D. Mangindaan, K. Khoiruddin, I.G. Wenten, Nanofiltration membrane cross-linked by m-phenylenediamine for dye removal from textile wastewater, *Polym. Adv. Technol.*, 30 (2019) 360–367.
7. H. Qian, Q. Hou, G. Yu, Y. Nie, C. Bai, X. Bai, M. Ju, Enhanced removal of dye from wastewater by Fenton process activated by core-shell NiCo₂O₄@FePc catalyst, *J. Clean. Prod.*, 273 (2020) 123028.
8. Y.S. Woo, M. Rafatullah, A.F.M. Al-Karkhi, T.T. Tow, Removal of Terasil Red R dye by using Fenton oxidation: a statistical analysis, *Desalin. Water Treat.*, 52 (2014) 4583–4591.
9. D. Ozturk, A.E. Yilmaz, Treatment of slaughterhouse wastewater with the electrochemical oxidation process: Role of operating parameters on treatment efficiency and energy consumption, *J. Water Process Eng.*, 31 (2019).
10. P. Hou, C. Shi, L. Wu, X. Hou, Chitosan/hydroxyapatite/Fe₃O₄ magnetic composite for metal-complex dye AY220 removal: Recyclable metal-promoted Fenton-like degradation, *Microchem. J.*, 128 (2016) 218–225.

11. N.C. Fernandes, L.B. Brito, G.G. Costa, S.F. Taveira, M.S.S. Cunha-Filho, G.A.R. Oliveira, R.N. Marreto, Removal of azo dye using Fenton and Fenton-like processes: Evaluation of process factors by Box–Behnken design and ecotoxicity tests, *Chem. Biol. Interact.*, (2018).
12. G. Ozgenc, M. Atakay, B. Salih, B. Zumreoglu-Karan, G. Elmaci, Degradation of Crystal Violet Dye from Waters by Layered MnO₂ and Nanocomposite-MnO₂@MnFe₂O₄ Catalysts, *Hacettepe J. Biol. Chem.*, (2017).
13. B. Bianco, I. De Michelis, F. Vegliò, Fenton treatment of complex industrial wastewater: Optimization of process conditions by surface response method, *J. Hazard. Mater.*, 186 (2011) 1733–1738.
14. J. Ma, W. Song, C. Chen, W. Ma, J. Zhao, Y. Tang, Fenton degradation of organic compounds promoted by dyes under visible irradiation, *Environ. Sci. Technol.*, (2005).
15. H. Sun, G. Xie, D. He, L. Zhang, Ascorbic acid promoted magnetite Fenton degradation ofalachlor: Mechanistic insights and kinetic modeling, *Appl. Catal. B Environ.*, 267 (2020) 118383.
16. R. Zhu, Y. Zhu, H. Xian, L. Yan, H. Fu, G. Zhu, Y. Xi, J. Zhu, H. He, C.N.T.s/ferrihydrite as a highly efficient heterogeneous Fenton catalyst for the degradation of bisphenol A: The important role of C.N.T.s in accelerating Fe(III)/Fe(II) cycling, *Appl. Catal. B Environ.*, 270 (2020).
17. A.R.D. Ahmad, S.S. Imam, W. Da Oh, R. Adnan, Fenton Degradation of Ofloxacin Using a Montmorillonite–Fe₃O₄ Composite, *Catalysts*, 11 (2021) 177.
18. S. Xin, G. Liu, X. Ma, J. Gong, B. Ma, Q. Yan, Q. Chen, D. Ma, G. Zhang, M. Gao, Y. Xin, High efficiency heterogeneous Fenton-like catalyst biochar modified CuFeO₂ for the degradation of tetracycline: Economical synthesis, catalytic performance and mechanism, *Appl. Catal. B Environ.*, 280 (2021) 119386.
19. T. Bayram, S. Bucak, D. Ozturk, BR13 dye removal using sodium dodecyl sulfate modified montmorillonite: Equilibrium, thermodynamic, kinetic and reusability studies, *Chem. Eng. Process. - Process Intensif.*, 158 (2020) 108186.
20. A. Kausar, M. Iqbal, A. Javed, K. Aftab, Z. i. H. Nazli, H.N. Bhatti, S. Nouren, Dyes adsorption using clay and modified clay: A review, *J. Mol. Liq.*, (2018).
21. R.M. Zakaria, I. Hassan, M.Z. El-Abd, Y.A. El-Tawil, Lactic acid removal from wastewater by using different types of activated clay, in: *Thirteen. Int. Water Technol. Conf. (IWTC)*, Hurghada, Citeseer, 2009: pp. 403–416.
22. M. Zhang, G. Pan, D. Zhao, G. He, XAFS study of starch-stabilized magnetite nanoparticles and surface speciation of arsenate, *Environ. Pollut.*, (2011).
23. K. Kalantari, M.B. Ahmad, K. Shamel, M.Z. Bin Hussein, R. Khandanlou, H. Khanehzaei, Size-Controlled Synthesis of Fe₃O₄ Magnetic Nanoparticles in the Layers of Montmorillonite, *J. Nanomater.*, 2014 (2014) 1–9.
24. L. Ma, S.I. Rathnayake, H. He, R. Zhu, J. Zhu, G.A. Ayoko, J. Li, Y. Xi, In situ sequentially generation of acid and ferrous ions for environmental remediation, *Chem. Eng. J.*, (2016).
25. A.D. Eaton, L.S. Clesceri, E. Rice, A.E. Greenbaerg, M.A.H. Franson, *Standard Methods for Examination of Water and Wastewater: Centennial Edition*, 2005.
26. F.E. Torun, I. Cengiz, S. Kul. Zeytin karasuyunun ileri oksidasyon prosesleri ile arıtımının incelenmesi, *İğdır Üniversitesi Fen Bilimleri Enstitüsü Dergisi*, (2020).
27. I. Talinli, G.K. Anderson. Interference of hydrogen peroxide on the standard cod test, *Water Res.*, (1992).
28. C.T. Benatti, C.R.G. Tavares, T.A. Guedes. Optimization of Fenton's oxidation of chemical laboratory wastewaters using the response surface methodology. *J. Environ. Manage.*, (2006).
29. J. Chang, J. Ma, Q. Ma, D. Zhang, N. Qiao, M. Hu, H. Ma, Adsorption of methylene blue onto Fe₃O₄/activated montmorillonite nanocomposite, *Appl. Clay Sci.*, 119 (2016) 132–140.
30. S.M. Lee, D. Tiwari, Organo and inorgano-organo-modified clays in the remediation of aqueous solutions: An overview, *Appl. Clay Sci.*, 59–60 (2012) 84–102.
31. T. Bayram, S. Bucak, D. Ozturk, BR13 dye removal using sodium dodecyl sulfate modified montmorillonite: Equilibrium, thermodynamic, kinetic and reusability studies, *Chem. Eng. Process. - Process Intensif.*, 158 (2020).
32. K.G. Bhattacharyya, S. Sen Gupta, Adsorption of Fe(III), Co(II) and Ni(II) on ZrO–kaolinite and ZrO–montmorillonite surfaces in aqueous medium, *Colloids Surfaces A Physicochem. Eng. Asp.*, 317 (2008) 71–79.
33. Y. Kim, Y.K. Kim, J.H. Kim, M.S. Yim, D. Harbottle, J.W. Lee, Synthesis of functionalized porous montmorillonite via solid-state NaOH treatment for efficient removal of cesium and strontium ions, *Appl. Surf. Sci.*, (2018).
34. P. Lu, J.L. Zhang, Y.L. Liu, D.H. Sun, G.X. Liu, G.Y. Hong, J.Z. Ni, synthesis and characteristic of the Fe₃O₄@SiO₂@Eu(D.B.M.)₃-2H₂O/SiO₂ luminomagnetic microspheres with core-shell structure, *Talanta*. (2010).
35. J.A. Lopez, F. González, F.A. Bonilla, G. Zambrano, M.E. Gómez, Synthesis and characterization of Fe₃O₄ magnetic nanofluid, *Rev. Latinoam. Metal. y Mater.*, (2010).
36. G.R. Mahdavinia, S. Hasanpour, L. Behrouzi, H. Sheykhoie, Study on adsorption of Cu(II) on magnetic starch- g-polyamidoxime/montmorillonite/Fe₃O₄ nanocomposites as novel chelating ligands, *Starch - Stärke.*, 68 (2016) 188–199.
37. J. Wang, G. Liu, Y. Liu, C. Zhou, Y. Wu, Photocatalytic Degradation of Methyl Orange by Fe₂O₃–Fe₃O₄ Nanoparticles and Fe₂O₃–Fe₃O₄–Montmorillonite Nanocomposites, *CLEAN - Soil, Air, Water.*, 45 (2017) 1600472.
38. S. Jebri, R. Khanfir Ben Jenana, C. Dridi, Green synthesis of silver nanoparticles using Melia azedarach leaf extract and their antifungal activities: In vitro and in vivo, *Mater. Chem. Phys.*, 248 (2020) 122898.
39. M. Jayapriya, D. Dhanasekaran, M. Arulmozhi, E. Nandhakumar, N. Senthilkumar, K. Sureshkumar, Green synthesis of silver nanoparticles using Piper longum catkin extract irradiated by sunlight: antibacterial and catalytic activity, *Res. Chem. Intermed.*, 45 (2019) 3617–3631.
40. Y. Akinay, F. Hayat, B. Çolak, Absorbing properties and structural design of P.V.B./Fe₃O₄ nanocomposite, *Mater. Chem. Phys.*, 229 (2019) 460–466.
41. H. Niu, P. Liu, F. Qin, X.L. Liu, Y. Akinay, PEDOT coated Cu-BTC metal-organic frameworks decorated with Fe₃O₄ nanoparticles and their enhanced electromagnetic wave absorption, *Mater. Chem. Phys.*, 253 (2020) 123458.
42. M. Danaei, M. Dehghankhold, S. Ataei, F. Hasanzadeh Davarani, R. Javanmard, A. Dokhani, S. Khorasani, M. Mozafari, Impact of Particle Size and Polydispersity Index on the Clinical Applications of Lipidic Nanocarrier Systems, *Pharmaceutics*, 10 (2018) 57.
43. N.R. Abdelsalam, M.M.G. Fouda, A. Abdel-Megeed, J. Ajarem, A.A. Allam, M.E. El-Naggar, Assessment of silver nanoparticles decorated starch and commercial zinc nanoparticles with respect to their genotoxicity on onion, *Int. J. Biol. Macromol.*, 133 (2019) 1008–1018.

44. A. Doweck, L.M.M. Lê, T. Rohmer, F.-X. Legrand, H. Remita, I. Lampre, A. Tfayli, M. Lavielle, E. Caudron, A mathematical approach to deal with nanoparticle polydispersity in surface enhanced Raman spectroscopy to quantify antineoplastic agents, *Talanta*, 217 (2020) 121040.
45. Q.U. Ain, U. Rasheed, M. Yaseen, H. Zhang, Z. Tong, Superior dye degradation and adsorption capability of polydopamine modified Fe₃O₄-pillared bentonite composite, *J. Hazard. Mater.*, 397 (2020) 122758.
46. J. Hua, M. Huang, Heterogeneous Fenton-like degradation of EDTA in an aqueous solution with enhanced COD removal under neutral pH, *Water Sci. Technol.*, 81 (2020) 2432–2440.
47. X. Li, K. Cui, Z. Guo, T. Yang, Y. Cao, Y. Xiang, H. Chen, M. Xi, Heterogeneous Fenton-like degradation of tetracyclines using porous magnetic chitosan microspheres as an efficient catalyst compared with two preparation methods, *Chem. Eng. J.* 379 (2020) 122324.,
48. B. Guo, T. Xu, L. Zhang, S. Li, A heterogeneous fenton-like system with green iron nanoparticles for the removal of bisphenol A: Performance, kinetics and transformation mechanism, *J. Environ. Manage.*, 272 (2020) 111047.
49. I. Mironyuk, T. Tatarchuk, H. Vasylyeva, V.M. Gun'ko, I. Mykytyn, Effects of chemisorbed arsenate groups on the mesoporous titania morphology and enhanced adsorption properties towards Sr(II) cations, *J. Mol. Liq.*, (2019).
50. V. Chittal, M. Gracias, A. Anu, P. Saha, K. V. Bhaskara Rao, Biodecolorization and biodegradation of azo dye reactive orange-16 by marine nocardiosis sp., *Iran. J. Biotechnol.*, 17 (2019) 18–26.
51. A.A. Telke, D.C. Kalyani, V. V. Dawkar, S.P. Govindwar, Influence of organic and inorganic compounds on oxidoreductive decolorization of sulfonated azo dye C.I. Reactive Orange 16, *J. Hazard. Mater.*, 172 (2009) 298–309.
52. M.G. Larson, *Analysis of Variance, Circulation*, 117 (2008) 115–121.
53. H.Y. Xu, S.Y. Qi, Y. Li, Y. Zhao, J.W. Li, Heterogeneous Fenton-like discoloration of Rhodamine B using natural schorl as catalyst: Optimization by response surface methodology, *Environ. Sci. Pollut. Res.*, 20 (2013) 5764–5772.
54. S. Hussain, E. Aneggi, D. Goi, Catalytic activity of metals in heterogeneous Fenton-like oxidation of wastewater contaminants: a review, *Environ. Chem. Lett.*, 1 (2021) 3.
55. I.D. Boateng, X.M. Yang, Process optimization of intermediate-wave infrared drying: Screening by Plackett–Burman; comparison of Box–Behnken and central composite design and evaluation: A case study, *Ind. Crops Prod.*, 162 (2021) 113287.
56. T. Şahan, D. Öztürk, Investigation of Pb(II) adsorption onto pumice samples: Application of optimization method based on fractional factorial design and response surface methodology, *Clean Technol. Environ. Policy.*, 16 (2014) 819–831.
57. S.S. Kashyap, P.R. Gogate, S.M. Joshi, Ultrasound assisted synthesis of biodiesel from karanja oil by interesterification: Intensification studies and optimization using RSM, *Ultrason. Sonochem.* 50 (2019) 36–45.
58. C.C. Nwobi-Okoye, M.K. Anyichie, C.U. Atuanya, RSM and ANN Modeling for Production of Newbouldia Laevies Fibre and Recycled High Density Polyethylene Composite: Multi Objective Optimization Using Genetic Algorithm, *Fibers Polym.* 21 (2020) 898–909.
59. S. Chamoli, ANN and RSM approach for modeling and optimization of designing parameters for a v down perforated baffle roughened rectangular channel, *Alexandria Eng. J.*, 54 (2015) 429–446.
60. M.O. Akinwande, H.G. Dikko, A. Samson, Variance Inflation Factor: As a Condition for the Inclusion of Suppressor Variable(s) in Regression Analysis, *Open J. Stat.*, 05 (2015) 754–767.
61. D. Ozturk, E. Dagdas, B.A. Fil, M.J.K. Bashir, Central composite modeling for electrochemical degradation of paint manufacturing plant wastewater: One-step/two-response optimization, *Environ. Technol. Innov.*, 21 (2020) 101264.
62. M.Z. Hassan, S.M. Sapuan, S.A. Roslan, S.A. Aziz, S. Sarip, Optimization of tensile behavior of banana pseudo-stem (Musa acuminata) fiber reinforced epoxy composites using response surface methodology, *J. Mater. Res. Technol.*, (2019).
63. M.A. Barakat, R. Kumar, E.C. Lima, M.K. Seliem, Facile synthesis of muscovite-supported Fe₃O₄ nanoparticles as an adsorbent and heterogeneous catalyst for effective removal of methyl orange: Characterization, modelling, and mechanism, *J. Taiwan Inst. Chem. Eng.*, 119 (2021) 146–157.
64. A. Mashayekh-Salehi, K. Akbarmojeni, A. Roudbari, J. Peter van der Hoek, R. Nabizadeh, M.H. Dehghani, K. Yaghmaeian, Use of mine waste for H₂O₂-assisted heterogeneous Fenton-like degradation of tetracycline by natural pyrite nanoparticles: Catalyst characterization, degradation mechanism, operational parameters and cytotoxicity assessment, *J. Clean. Prod.*, 291 (2021) 125235.
65. G. Imoberdorf, M. Mohseni, Degradation of natural organic matter in surface water using vacuum-UV irradiation, *J. Hazard. Mater.*, 186 (2011) 240–246.
66. J. Sharma, I.M. Mishra, V. Kumar, Degradation and mineralization of Bisphenol A (B.P.A.) in aqueous solution using advanced oxidation processes: UV/H₂O and UV/S₂O₈²⁻ oxidation systems, *J. Environ. Manage.*, 156 (2015) 266–275.
67. N. Sétifi, N. Debbache, T. Sehili, O. Halimi, Heterogeneous Fenton-like oxidation of naproxen using synthesized goethite-montmorillonite nanocomposite, *J. Photochem. Photobiol. A Chem.* 370 (2019) 67–74.
68. A. Tolba, M. Gar Alalm, M. Elsamadony, A. Mostafa, H. Afify, D.D. Dionysiou, Modeling and optimization of heterogeneous Fenton-like and photo-Fenton processes using reusable Fe₃O₄-MWCNTs, *Process Saf. Environ. Prot.* 128 (2019) 273–283.
69. M. Arshadi, M.K. Abdolmaleki, F. Mousavinia, A. Khalafi-Nezhad, H. Firouzabadi, A. Gil, Degradation of methyl orange by heterogeneous Fenton-like oxidation on a nano-organometallic compound in the presence of multi-walled carbon nanotubes, *Chem. Eng. Res. Des.* 112 (2016) 113–121.
70. H.L. So, K.Y. Lin, W. Chu, Triclosan removal by heterogeneous Fenton-like process: Studying the kinetics and surface chemistry of Fe₃O₄ as catalyst, *J. Environ. Chem. Eng.* 7 (2019) 103432.
71. C. Ma, Z. He, S. Jia, X. Zhang, S. Hou, Treatment of stabilized landfill leachate by Fenton-like process using Fe₃O₄ particles decorated Zr-pillared bentonite, *Ecotoxicol. Environ. Saf.* 161 (2018) 489–496.
72. C. Shao-Hua, D.-Y. Du, degradation of n-butyl xanthate using fly ash as heterogeneous Fenton-like catalyst, *J. Cent. South Univ.* 21 (2014) 1448–1452. I. Hirsch, E. Prell, M. Weiwad, Assessment of cell death studies by monitoring hydrogen peroxide in cell culture, *Anal. Biochem.* 456 (2014) 22–24.
73. I. Hirsch, E. Prell, M. Weiwad, Assessment of cell death studies by monitoring hydrogen peroxide in cell culture, *Anal. Biochem.* 456 (2014) 22–24.